

Preliminary Results of Source Parameter Inversion of Earthquake Sequences Induced by Hydraulic Fracturing in the Kiskatinaw Area, Northeastern British Columbia (Parts of NTS 093P, 094A)

M.P. Roth¹, Ruhr University Bochum, Bochum, Germany, marco.roth@rub.de

K.B. Kemna, Ruhr University Bochum, Bochum, Germany

R.M. Harrington, Ruhr University Bochum, Bochum, Germany

Y. Liu, McGill University, Montréal, Quebec

Roth, M.P., Kemna, K.B., Harrington, R.M. and Liu, Y. (2021): Preliminary results of source parameter inversion of earthquake sequences induced by hydraulic fracturing in the Kiskatinaw area, northeastern British Columbia (parts of NTS 093P, 094A); *in* Geoscience BC Summary of Activities 2020: Energy and Water, Geoscience BC, Report 2021-02, p. 67–80.

Introduction

The occurrence of earthquakes in relation to hydraulic fracturing (HF) during hydrocarbon production is of considerable scientific interest on a global scale (Foulger et al., 2018). Especially in historically seismically quiescent regions, HF-induced events can increase the natural seismic hazard in the time period of anthropogenic interference. The significance of increased seismic hazard associated with HF operations was illustrated by several damaging induced events, including an M_L 5.7 earthquake in the Sichuan Basin on December 16, 2018 (Lei et al., 2019). Nevertheless, to ensure the energy needs of the general public, research is needed on the interaction between energy production and earthquakes induced by fluid injection (McGarr et al., 2015). As an example, the Western Canada Sedimentary Basin (WCSB) has experienced an increasing number of M_3+ events in the last decade, which correlates with an increase in oil and gas production (Atkinson et al., 2016). Particularly the Montney Formation, a major shale-gas play in northeastern British Columbia (BC) and northwestern Alberta, is capable of hosting events of magnitude 4+, such as an M_w 4.6 on August 17, 2015 near Fort St. John (Babaie Mahani et al., 2017; Wang et al., 2020) and an M_w 4.2 (M_L 4.5) on November 30, 2018 near Dawson Creek (Babaie Mahani et al., 2019; Peña Castro et al., 2020).

Recently, Roth et al. (2020) found a high temporal and spatial correlation between HF operations and the occurrence of earthquakes in the Kiskatinaw area (Figure 1), a region extending between Fort St. John and Dawson Creek that covers parts of the Montney Formation (Figure 1, purple

area on inset map). The linear features evident in the spatial distribution of induced earthquakes align primarily at low angles to S_H , the orientation of maximum horizontal compressive stress. The alignment is interpreted as a fault orientation and is therefore consistent with strike-slip faulting on optimally oriented slip surfaces. Further estimations of focal-mechanism solutions (FMSs) of moderate-sized events in the study area suggest the occurrence of strike-slip, as well as thrust-faulting, events (Onwuemeka et al., 2019; Babaie Mahani et al., 2020; Peña Castro et al., 2020). This paper focuses on the inversion of earthquake-source parameters (i.e., FMS, seismic moment and stress drop) to evaluate possible activated fault planes and to investigate the scaling relations for repeating induced events in the study area.

Earthquake Catalogue

The earthquakes considered in this study are based on an automated earthquake catalogue by Roth et al. (2020) extending to the time period from July 12, 2017 to July 31, 2020. The catalogue contains a total of 8302 events (circles in Figure 1) detected with a short-term average/long-term average (STA/LTA) trigger that includes a 3–20 Hz, 4th order Butterworth bandpass filter, an STA duration of 0.2 s, an LTA duration of 10 s, a triggering threshold of 2.5 and a detriggering threshold of 1.5 for P-wave first arrivals, as well as a 3–12 Hz, 3rd order Butterworth bandpass filter and an Akaike information-criterion algorithm for S-wave first arrivals. All phase arrivals are reviewed by an analyst. This study uses a total of 25 stations (triangles in Figure 1) operated by Ruhr University Bochum (RUB), McGill University (MGU) and Natural Resources Canada (NRCan), although several stations were not operating from the starting time of the catalogue (Table 1).

Focal-Mechanism Inversion

This study uses the probabilistic earthquake-source inversion framework ‘Grond’ (Dahm et al., 2018) to estimate the

¹The lead author is a 2020 Geoscience BC Scholarship recipient.

This publication is also available, free of charge, as colour digital files in Adobe Acrobat® PDF format from the Geoscience BC website: <http://geosciencebc.com/updates/summary-of-activities/>.

FMS for 11 representative earthquakes with a magnitude of M_L 2.7+ in the earthquake catalogue. The FMS is computed for a variety of earthquake sequences based on the waveform-similarity clustering in Roth et al. (2020). Grond inverts for the optimal hypocentral location and moment tensor by applying a bootstrap technique on a dataset of fully inverted waveforms that are compared to a synthetic dataset modelled from Green's functions. These were previously calculated by 'Qseis' (Wang, 1999) and 'Fomosto' (Heimann et al., 2017) using the same velocity model as in Roth et al. (2020; this velocity model is used throughout

this study). The optimal FMS is calculated based on the time and frequency domains, as well as the waveform envelopes. The initial Green's functions are modelled up to 10 Hz, which allows fitting of the full waveforms in a low-frequency band up to 5 Hz, the Nyquist frequency. For each event, several inversions are run in varying frequency bands to compute an FMS with a minimum mean bootstrap misfit of at least <0.65 to be considered for this study, a value dependent on the individual dataset determined by empirical testing. In general, the comparison of modelled versus observed waveforms is the crucial factor in judging

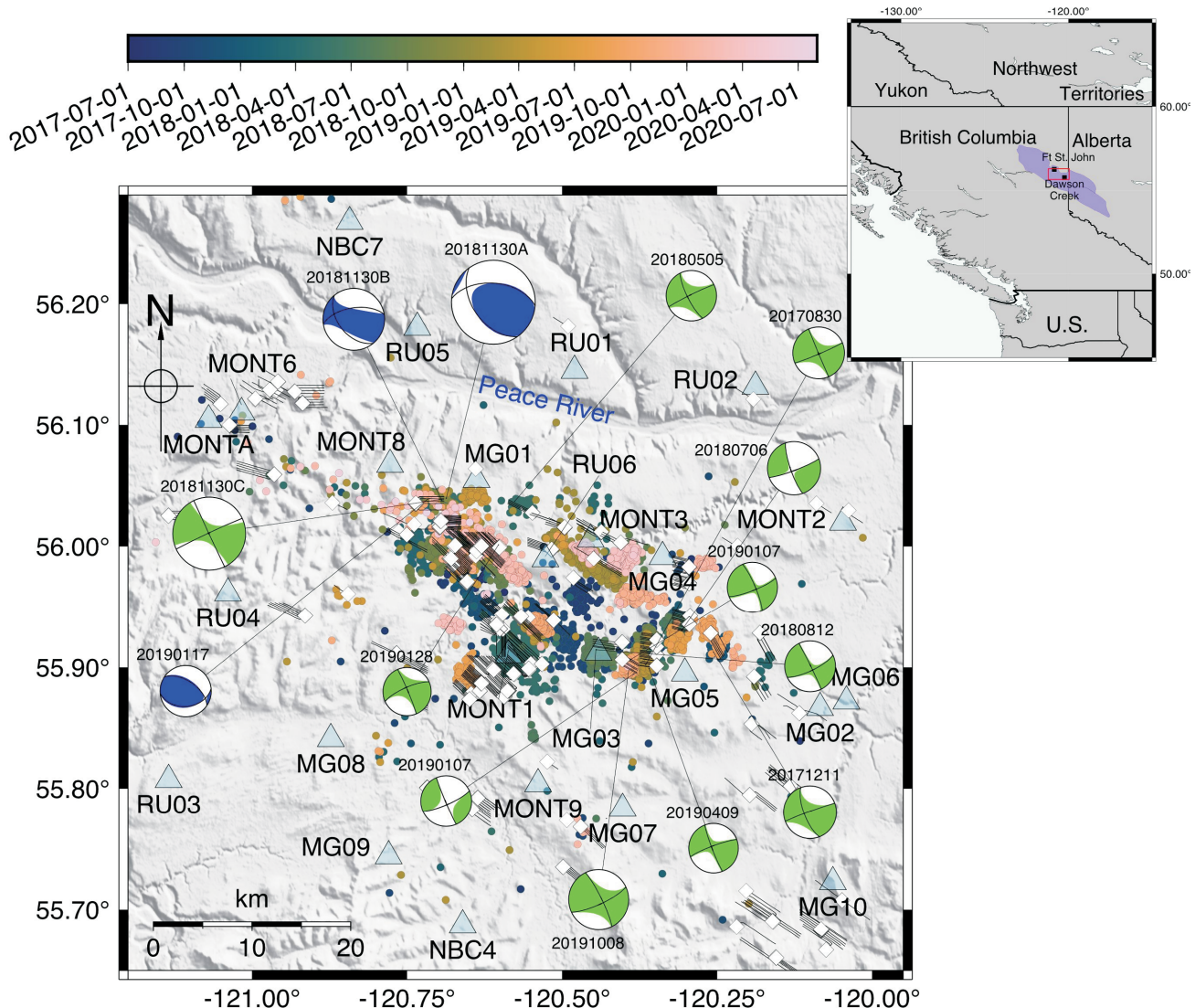


Figure 1. Overview of the Kiskatinaw area in northeastern British Columbia, indicated by the red box on the inset map. The purple-highlighted area on the inset map denotes the shape of the Montney Formation, as reported by the BC Oil and Gas Commission (BCOGC; last accessed October 2018), and the Alberta Energy Regulator (AER; last accessed May 2020). Blue triangles denote stations. Stations starting with RU are operated by Ruhr University Bochum (RUB), those starting with MG are operated by McGill University (MGU) and those starting with MONT and NBC are operated by Natural Resources Canada (NRCan). Circles show the epicentre of earthquake locations, colour coded by origin time. Focal-mechanism plots illustrate the fault type of some representative events in the catalogue, labelled by their respective origin date (YYYYMMDD; blue for dominantly thrust faulting, green for dominantly strike-slip faulting). White diamonds represent HF wells operating in the catalogue's time period, with black lines indicating the trajectories of the horizontal wells (injection data are provided by the BC Oil and Gas Commission; last accessed August 13, 2020). Additional wells might be updated by the respective operators.

Table 1. Overview of all stations, with their locations, used in this study. Stations with network code XL are operated by MGU and RUB, and those with network code 1E and CN by NRCan. The start time shows the beginning of data collection, while the end date gives the supposed date of removal. Station information is archived on the Incorporated Research Institutions for Seismology (IRIS) Data Management Center (www.iris.edu; last accessed October 2020).

Network	Station name	Latitude	Longitude	Start date	End date
XL	MG01	56.05484	-120.637993	2017-Jun-19	2020-Dec-31
XL	MG02	55.866791	-120.083992	2017-Jun-14	2020-Dec-31
XL	MG03	55.912151	-120.44136	2017-Jun-16	2020-Dec-31
XL	MG04	55.99136	-120.338043	2017-Jun-17	2020-Dec-31
XL	MG05	55.895142	-120.301949	2017-Jun-15	2020-Dec-31
XL	MG06	55.87212	-120.041481	2018-Jun-22	2020-Dec-31
XL	MG07	55.783562	-120.40242	2017-Aug-02	2020-Dec-31
XL	MG08	55.84116	-120.87307	2017-Jun-14	2020-Dec-31
XL	MG09	55.74419	-120.779617	2017-Jun-18	2020-Dec-31
XL	MG10	55.722851	-120.063347	2019-Oct-01	2020-Dec-31
XL	MG11	55.86168	-120.11468	2020-Sep-01	2022-Jun-30
XL	RU01	56.145069	-120.480042	2019-Jul-30	2020-Dec-31
XL	RU02	56.131989	-120.188187	2019-Jul-30	2020-Dec-31
XL	RU03	55.807442	-121.134506	2019-Sep-26	2020-Dec-31
XL	RU04	55.961369	-121.038788	2019-Oct-03	2020-Dec-31
XL	RU05	56.180611	-120.733391	2019-Oct-04	2020-Dec-31
XL	RU06	55.98959	-120.526909	2019-Sep-29	2020-Dec-31
1E	MONT1	55.910149	-120.58654	2018-Oct-01	2021-Oct-01
1E	MONT2	56.019718	-120.046967	2018-Oct-01	2021-Oct-01
1E	MONT3	56.005779	-120.45388	2018-Oct-01	2021-Oct-01
1E	MONT6	56.110291	-121.016991	2018-Oct-03	2021-Oct-01
1E	MONT8	56.06731	-120.777428	2019-Jul-15	2021-Oct-01
1E	MONT9	55.803902	-120.538757	2019-Oct-07	2021-Oct-01
1E	MONTA	56.104321	-121.070038	2019-Oct-05	2021-Oct-01
CN	NBC4	55.687279	-120.66024	2013-Mar-01	2599-Dec-31
CN	NBC7	56.267792	-120.842621	2014-Aug-10	2599-Dec-31

the quality of the calculated FMS. In addition to the 11 FMSs calculated in this study, three have been included from Peña Castro et al. (2020).

Spectral Analysis

Spectral-source parameters of 8302 earthquakes were estimated based on their waveforms. The source parameter inversion to determine long-period spectral amplitude and corner frequency is based on two methods, the single spectrum and the spectral-ratio calculation, both of which are described below. As the S-waves typically have a higher signal-to-noise ratio (SNR), only they are used for this study. To estimate a time window covering the complete S-wave signal, an initial theoretical corner frequency ($f_{c,\text{initial}}$) was estimated based on the local magnitude reported in the catalogue, the relation of Ross et al. (2016) to estimate a moment magnitude, a lower-bound stress drop of 0.1 MPa, and the constant $k = 0.26$ for a singular crack expanding radially at a rupture speed of 90% of the shear-wave velocity (after recent analyses by Kaneko and Shearer, 2014).

Therefore, $t = 2/f_{c,\text{initial}}$ is used as the window length. The choice of 0.1 MPa as a stress-drop value will lead to a lower boundary for the corner-frequency estimation and, due to the inverse relation to t , the time window will therefore be long enough to guarantee coverage of the complete phase. Although longer time windows are reported (e.g., Ross and Ben-Zion, 2016), this study will continue with twice the inverse of the estimated corner frequency, as this relation will lead to $t \approx 1$ s for M_L 2.5 events at the typical depth of 2 km (Roth et al., 2020). For smaller events reported in the catalogue where the time window would be even shorter, a one-second time window is used to keep enough data points in the waveform.

Single-Spectrum Method

This study employs the waveforms for each available pick beginning at 25% of the window length before the phase arrival, and a corresponding noise window with the same length, one-time window before the P-arrival. If no P-arrival is detected, 5 s before the origin time is used. In the

next step, the single spectra of individual components are calculated using a multitaper approach (Prieto et al., 2009). To enhance the signal, the vector sum of both horizontal components, if two components were available due to the absence of data gaps, and a dynamically calculated time window are used. To avoid potential bias of the following curve fit toward higher frequencies, each spectrum is resampled using an equally spaced logarithmical sampling-size interval. Next, a numerical fit is estimated for the corner frequencies and the long-period spectral amplitude using the Boatwright source model (Boatwright, 1978),

$$\Omega(f) = \Omega_0 \frac{e^{-(\frac{\pi f t}{Q})}}{\left(1 + \left(\frac{f}{f_c}\right)^{\gamma n}\right)^{1/\gamma}}, \quad (1)$$

with the long-period spectral amplitude Ω_0 fixed to the maximum amplitude of the respective single spectrum, frequency f , the source-receiver travel time t as reported by the catalogue, the corner frequency f_c to be fitted, the high-frequency falloff rate n , the seismic attenuation Q (where Q and n will be fixed to one value, although recent studies point out lower uncertainties for a clustered- Q approach; Ko et al., 2012; Yu et al., 2020; see ‘Estimation of optimal parameter settings for Q and n ’ below), and a factor γ that controls the shape of the corner and is fixed at $\gamma = 2$ for the Boatwright source model. One single spectrum is considered to be fitted if its SNR exceeds a threshold of 3 for 1–30 Hz ($M_L < 3$), 1–20 Hz ($3 < M_L < 4$) or 1–15 Hz ($M_L > 4$), as the instrument response function is flat between 0.1 Hz and 45 Hz, with a sampling rate of 100 Hz. One example of the fitted spectrum and the corresponding waveforms is plotted in Figure 2.

Spectral-Ratio Method

A second method for calculating source parameters is the spectral-ratio method, which can be applied if two events of similar waveforms are located within approximately one source dimension defined by the larger event (Abercrombie, 2015), and recorded at the same station; the larger event of this pair is called the ‘target’ event and the smaller one the ‘empirical Green’s function’ (EGF; Hartzell, 1978). Dividing the two single spectra (Equation 1) to calculate the spectral ratio,

$$\Omega(f) = \frac{\Omega_0^{\text{target}}}{\Omega_0^{\text{EGF}}} \left[\frac{1 + \left(\frac{f}{f_c^{\text{EGF}}}\right)^{\gamma n}}{1 + \left(\frac{f}{f_c^{\text{target}}}\right)^{\gamma n}} \right]^{1/\gamma}, \quad (2)$$

cancels out instrument- and non-source-related effects, such as site effects, and leaves the source differences of the target and the EGF events. In this study, all events with a magnitude difference of at least 0.5 relative to the target event, a maximum distance of 5 km to the target event and a cross-correlation coefficient (CCC) of 0.8 or higher on one

channel of the closest station were considered as potential EGF. Although the relative magnitude difference between target event and EGF is sometimes reported to be at least 1.0 to ensure the amplitude ratio is high enough to differentiate the two corner frequencies (e.g., Hartzell, 1978), the lower difference is applied in order to avoid pre-emptively removing a large number of event pairs that may be viable, a practice that has already yielded significant results globally (Kwiatek et al., 2014; Harrington et al., 2015) and in the WCSB (Holmgren et al., 2019). The benefit of the smaller magnitude difference is a higher number of EGFs connected to the target event, which will be manually reviewed in a later stage of the analysis and ensures an adequate number of possible EGFs for the predominant small-magnitude events in the WCSB (Holmgren et al., 2019).

For calculating the CCC, a window length is chosen that covers the P- and S-wave arrival, as well as the coda, by starting 0.5 s before the P-wave onset and ending 1.8($t_S - t_P$) after the P-wave onset, where $t_S - t_P$ describes the difference in S and P arrival times. Calculating the CCC of full waveforms ensures that the overall waveform is similar, which requires a similar FMS for both events (Harrington et al., 2015; Ruscic et al., 2019). The additional CCC criterion, to link targets with EGFs, is a further argument for only linking similar events with each other. In the preliminary processing steps for the beginning of the catalogue, where fewer stations were operating simultaneously, more successful combined target-EGF pairs were found using a rather high CCC on the closest station only, presumably because the CCC will decrease for larger distances due to attenuating effects and a lower SNR. Besides, if the CCC is high on the closest station, it suggests a similar focal mechanism (Got et al., 1994). Furthermore, the minimum magnitude for target events was limited to $M_L 2$, and the individual SNRs must exceed the same threshold of 3 for 1–30 Hz to guarantee a high portion of S-wave signal in the processed time window. Otherwise, the desired corner frequency might be covered by seismic noise in the same frequency band. In this study, the corner frequency can be resolved at least up to 10–15 Hz (Abercrombie, 2014), and Abercrombie et al. (2017) and Ruhl et al. (2017) reported an even higher cut-off criterion (i.e., half to two-thirds of the upper frequency for SNR resolution, in the present case 15–20 Hz). The window length of both waveforms is equal to the estimated window length for the target event. To ensure a high quality of the spectral-ratio fits, a graphical user interface (GUI) was designed to visually inspect all spectral-ratio pairs and, if needed, manually adjust some fitting parameters.

Estimation of Optimal Parameter Settings for Q and n

To guarantee a fit according to Equation 1, which will only fit the corner frequency f_c and discharges potential numeri-

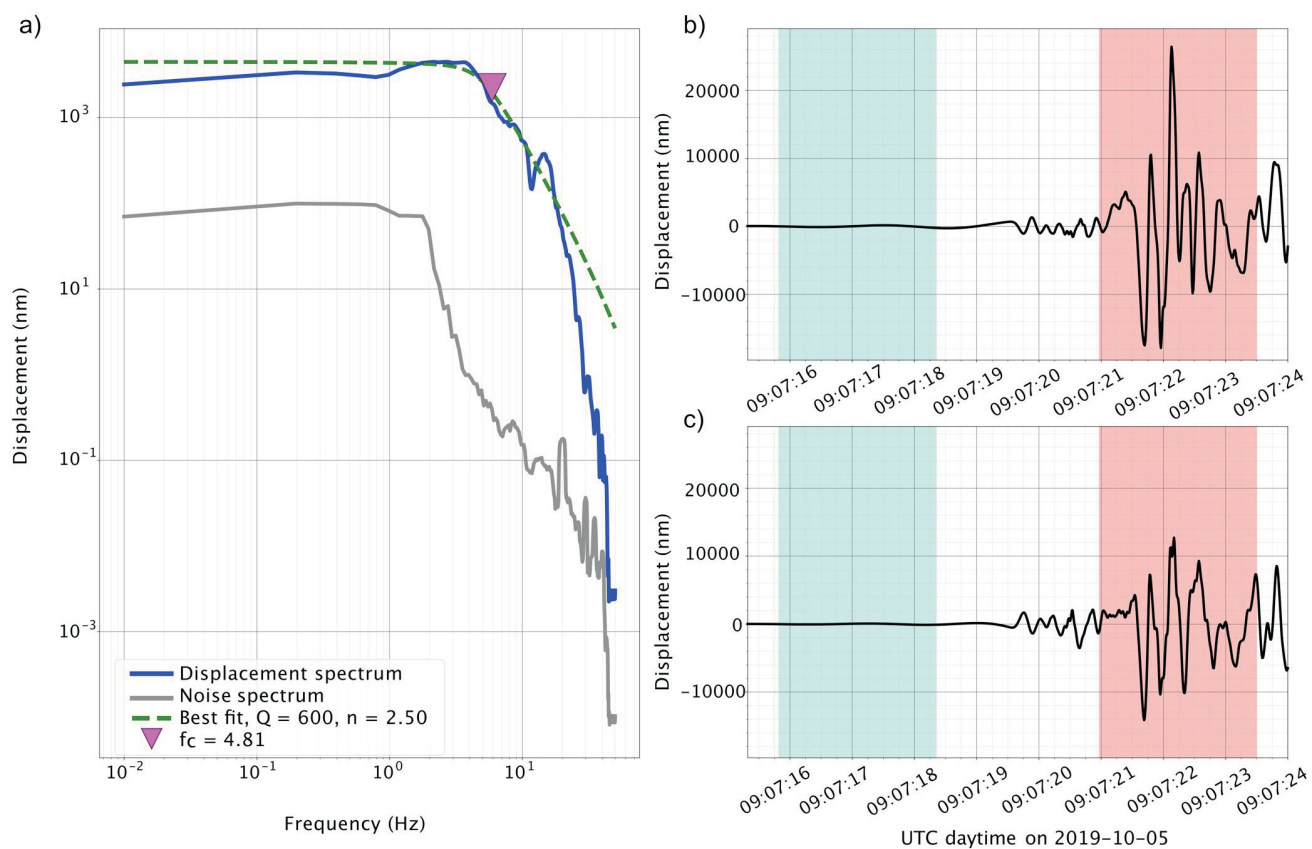


Figure 2. Example plot of one fitted single spectrum on station RU06 from an event with a magnitude of M_L 3.4 that occurred southeast of the study area on October 5, 2019: **a)** displacement spectrum (blue) of the signal (pink shading in parts b and c) and a fit using Equation 1 (green dashed line); grey line displays the noise level (blue shading in parts b and c) directly before the event happened; **b)** and **c)** displacement waveform on the north and east components of RU06, respectively.

cal trade-off effects between f_c , Q and n , constant values were chosen for Q and n . As Q describes the seismic attenuation, it is defined by rock properties. This study is limited to one region with rather uniform mechanical behaviour, as well as widespread HF operations affecting larger parts of the area. Furthermore, the high-frequency fall-off rate n is affected by rupture processes (i.e., duration time and fraction of stress drop; Brune, 1970), which are similar in this study area due to a high number of repetitive waveforms (Roth et al., 2020). Therefore, it was decided to keep both values constant. The values of the (Q , n) pair were calculated with the smallest overall misfit by a grid-search approach based on 2 066 064 individual fits for 13 n -values between 1.75 and 3.25 in a spacing of 0.125, and 56 Q -values between 250 and 3000 and a spacing of 50 for 2838 event-station pairs (Figure 3). The chosen events are a subset of 239 target events, where spectral ratios with multiple EGFs could be calculated in the later analysis step. The χ^2 -misfit was first calculated for each of the desired fits. As the misfit itself is not comparable to the misfit on other stations, it is necessary to norm the individual misfit to a reference misfit, which in this study is the Q - n pair of 1000 and 2, as used in previous spectral-analysis studies for the WCSB (Clerc et al., 2016; Holmgren et al., 2019; Wang et al.

2020), and afterwards calculate the mean misfit for all event-station pairs. The warm colours in Figure 3 show a relative decrease in misfit (i.e., an improvement of the model settings, which results in the chosen values for Q and n being 600 and 2.5, respectively). A study by Yu et al. (2020) had already showed a successful application for constant Q values according to the spatial distribution of induced events in the WCSB, where the authors calculated an apparent Q , representing the ray path in a layered Q structure.

Seismic Moment and Corner Frequency

The following steps describe how the source parameters are estimated from the previously fitted single spectra and spectral ratios. First, the seismic moment can be estimated for each of the events at each of the stations that exceeded the SNR of 3 by extracting the long-period spectral amplitude of the respective single spectra. Following the Brune (1970) relation, the seismic moment is defined by

$$M_0 = \frac{4\pi\rho\beta^3\Omega_0 R}{U_{\Phi\Theta}}, \quad (3)$$

with the shear-wave velocity β , the rock density ρ (where the value is between 2.46 and 2.86 g/cm³, depending on the

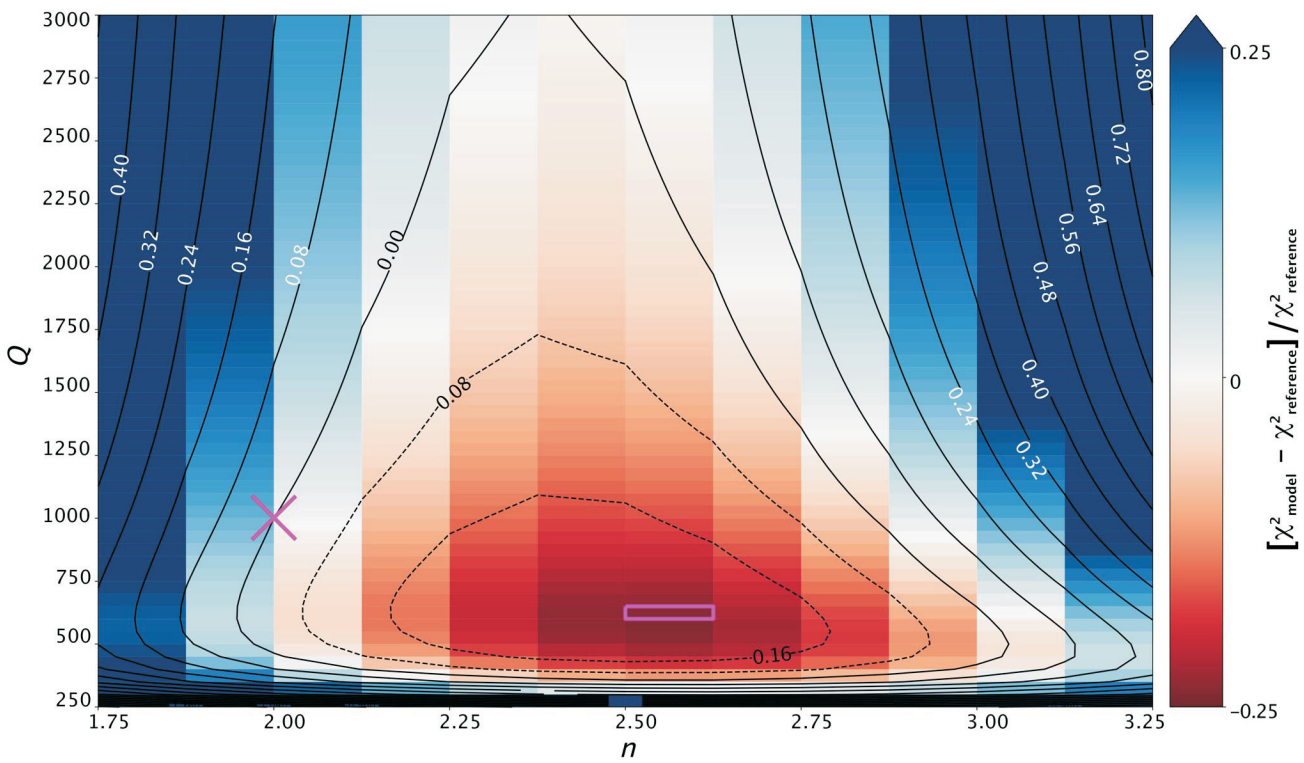


Figure 3. Relative χ^2 misfit variations of single spectra with different Q - n pairs for 239 chosen events on all possible stations, normalized on $Q = 1000$ and $n = 2.0$ (magenta cross). Warm colours denote a decrease in relative misfit (improvement of the fit) and cool colours an increase in relative misfit (worsening of the fit). Solid and dashed isolines show interpolations for the models with 8% increases and decreases, respectively, in relative misfit. The model used in this study is highlighted as a magenta box.

hypocentral depth), the source-receiver distance R , and the radiation pattern for S waves of $U_{\Phi\Theta} = 0.63$ (Aki and Richards, 2002). In this study, all events with a minimum of five successful fits (i.e., estimates of seismic moment and corner frequency on five stations) were considered. To calculate one seismic moment for the event, the jackknife mean, including the confidence level, is calculated from all station values of all estimates for Ω_0 (Prieto et al., 2007), where one estimate of Ω_0 is the maximum value of the respective single spectrum. The seismic moment is derived only from single-spectrum estimates, as Equation 2 does not contain a spectral amplitude isolated for the events.

To minimize the variables that need to be fitted into Equation 2, the low frequency level was set to the maximum of the observed spectral ratio, and $n = 2.5$. A target-EGF pair was considered if at least five spectral ratios were calculated. Next, all potential target-EGF pairs were stacked and evaluated by a newly developed GUI (Figure 4), which allows the analyst to add or remove single stations to or from the fit, and adapt the frequency band in which the fit should be calculated. For spectral ratios, where both fitted corner frequencies are close to each other and where the amplitude ratio between the lower- and upper-frequency portions is low, f_c^{target} is not distinct. To ensure that the second corner frequency f_c^{EGF} is not misinterpreted as the first corner frequency f_c^{target} by the numerical fit, the analyst can add a

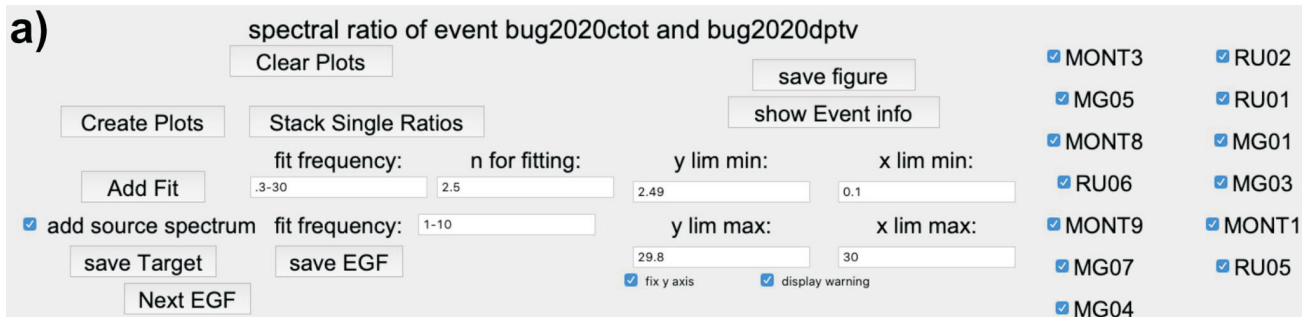
source spectrum (Brune, 1970), which is Equation 1 reduced by the attenuation term (i.e., the exponential term involving Q). If the fit of the target-EGF pair has an adequate shape, and f_c^{target} is resolvable, the analyst can decide to save or withdraw the pair. Figure 4 shows one example of a well-resolved spectral ratio. This study is limited to estimations of f_c^{target} only, as the magnitude range in the catalogue does not allow large differences between target and EGF magnitude, and f_c^{EGF} will probably exceed the frequency bandwidth-limitation of 10–15 Hz.

Stress-Drop Calculation

In the next step, the prior estimated corner frequency is used to calculate the stress drop of the specific event. While the seismic moment and the corner frequency describe the fault of an earthquake, the stress drop can give insights into the rupture process (i.e., stress relief due to the event). To derive the stress drop $\Delta\sigma$ from one single spectrum and spectral ratios, a model for a circular crack is used (Eshelby, 1957), specifically

$$\Delta\sigma = \frac{7}{16} \frac{M_0}{r^3}, \quad (4)$$

where r describes the fault radius for a circular crack, calculated from the radiated S-wave spectrum (Brune, 1970, 1971)



b)

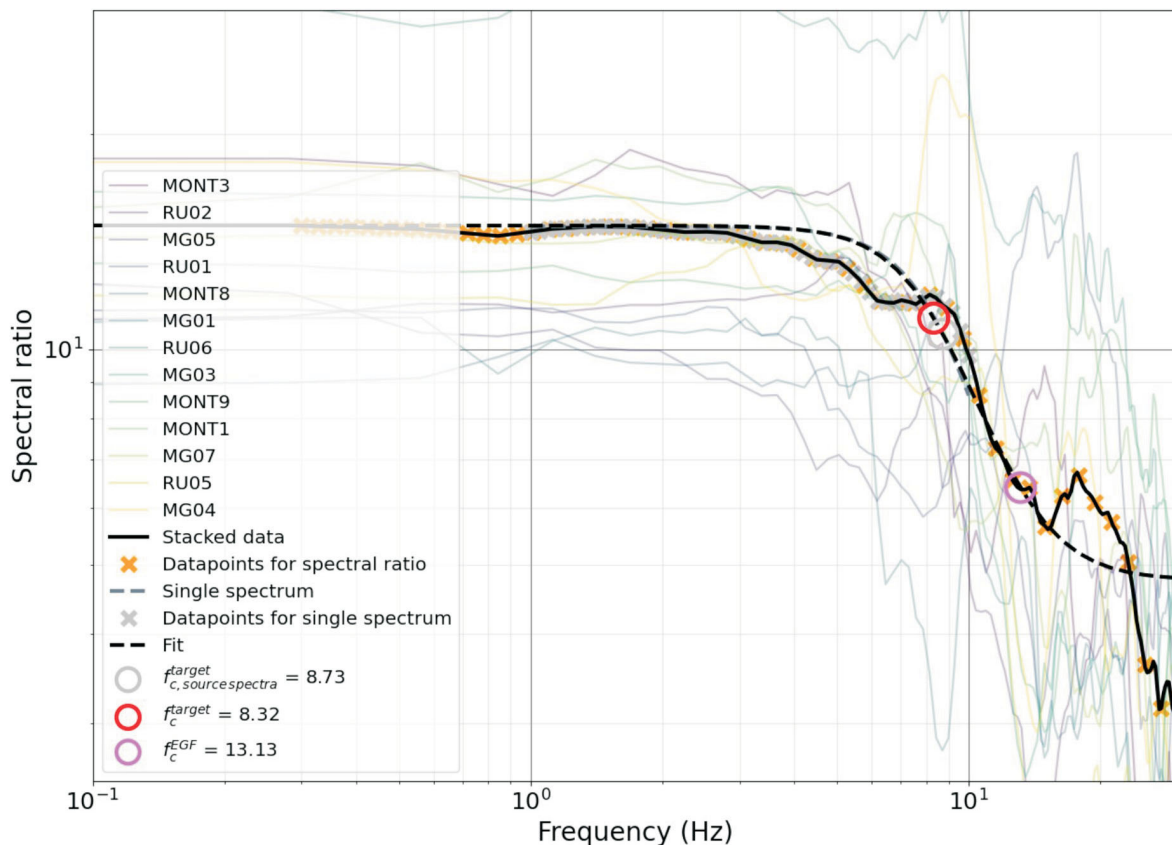


Figure 4. a) Menu bar of the GUI for one spectral-ratio pair of one M_L 3.1 target event (work ID 'bug2020ctot') and one M_L 2.0 EGF (bug2020dptv). The user can individually plot all spectral ratios ('Create Plots'), add the stack of all visible spectral ratios ('Stack Single Ratios') and add the fit, using Equation 2 ('Add Fit') for specific frequency bands. The x and y axes can be limited using the 'x lim' and 'y lim' windows, respectively. Deactivating individual checker boxes next to the stations starting with RU, MG or MONT can remove individual stations to be considered. The individual locations of the stations are provided in Figure 1 and Table 1. 'show Event info' can display the origins and magnitudes of the events. When the analyst confirms the quality of the fit, then the figure and the corner frequency for the target and for the EGF can be saved. **b)** Example plot of one fitted spectral-ratio pair. The coloured lines show individual spectral ratios on one station. The solid black line is the stack of all spectral ratios, while the dashed black line shows the determined best fit. Orange and grey crosses show the data points of the stack, which are considered for the fit using the spectral ratio (Equation 2) and the source spectrum, respectively. The red and purple circles highlight the corner frequencies for target and EGF, respectively, using Equation 2, while the grey circle can confirm the first corner frequency using the source spectrum.

$$r = \frac{\kappa\beta}{f_c}. \quad (5)$$

As the previous analytical steps may yield multiple values for f_c (due to multiple single spectra on various stations, or to multiple EGFs used for one target event), the mean value is always used. In the same way that corner frequencies were calculated individually using two methods (using the single spectra and the spectral ratios), individual stress-drop values can also be calculated with both methods. However, the seismic moment is calculated using only the single-spectrum approach.

Results

Figure 1 shows 14 focal-mechanism plots, three of which are from Peña Castro et al. (2020). The majority of events are dominated by a left-lateral, strike-slip faulting mechanism (11 out of 14), and the remaining events are dominated by a thrust-faulting mechanism. While the thrust-faulting events with magnitudes between M_L 4.5 and M_L 2.7 can only be observed close to Fort St. John in the northwestern part of the Kiskatinaw area, there is no clear trend for the distribution of strike-slip events, which have magnitudes between M_L 3.4 and M_L 2.8.

In total, 1772 of the 8002 events passed the quality-control criteria for deriving source parameters by fitting the single spectra, while 303 events could be used for the spectral-ratio method. Figure 5 shows a summary of the spectral-analysis results for both single spectra (blue and grey circles) and spectral ratios (green diamonds). Comparing the single-spectra results for the events for which spectral ratios could be calculated (blue circles) with the events for which the single-spectrum method was used (grey circles) shows the same scaling, but for different magnitude ranges, due to the fact that there are fewer EGFs and smaller SNRs for smaller magnitude target events. Figure 5a shows the scaling for stress drop versus seismic moment (or moment magnitude), where single spectra suggest an increase of stress drop with increasing seismic moment between roughly 10^{-1} MPa ($M_w \sim 1.5$) and 3×10^1 MPa ($M_w \sim 4.2$). Contrary to the single spectra, the spectral ratios highlight a scattering between 10^0 and 10^2 MPa, with no clear trend apparent. Furthermore, a higher number of events seem to be underestimated, as they are above the resolvable frequency content of the instrument (grey shading on Figure 5), while only a few events are higher than 13 Hz, the instrumental resolution limit that is dictated by the SNR threshold of 30 Hz.

Plotting the seismic moment (or moment magnitude) against the corner frequency (Figure 5b) shows a steep decrease of seismic moment with corner frequency. In addition, the stress drop scatters between 10^{-1} MPa and 10^1 MPa. Results from the spectral ratios do highlight a rather slight decrease of seismic moment with increasing

corner frequency, implying a constant stress drop between 10^0 MPa and 10^2 MPa, optimally at 10^1 MPa.

Discussion and Conclusion

The estimated focal mechanism of this study agrees with the general trend of focal mechanisms from previous studies (Onwuemeka et al., 2019; Babaie Mahani et al., 2020; Peña Castro et al., 2020). In addition, the left-lateral strike-slip faults from the focal-mechanism plots are consistent with the fault orientations at roughly 30° to S_H in Roth et al. (2020). The fact that no EGF fulfills the defined quality-control criteria for the M_L 4.5 suggests an isolated hypocentre for this particular mainshock, as suggested in Peña Castro et al. (2020). Two focal-mechanism solutions are observed in the northwestern part of the study area, close to the Peace River (Figure 1) and to the Fort St. John graben (e.g., Barclay et al., 1990; Davies, 1997; Eaton et al., 1999), suggesting thrust-faulting events and strike-slip events, whereas the southeastern part of the area hosts exclusively strike-slip events. The reason for this could be that the area close to the Fort St. John graben may host normal faults formed by graben building and basin infill, which can be reactivated as thrust faults in the current stress regime. In contrast, the southeastern part of the study area hosts solely shallow strike-slip events, perhaps due to the absence of potential deep receiver faults. A second natural source for existing thrust faults would be the thrust-faulting belt in the Rocky Mountain foreland (Pană and van der Pluijm, 2015), formed during the Laramide orogeny.

Another factor supporting the observation of two types of FMS in the same region may take into account the stress constraints from borehole data and focal-mechanism inversions in Fox Creek, Alberta (Shen et al., 2019): S_v could be larger than S_h for the shallower depths in the WCSB, resulting in strike-slip events, while S_h could be larger than S_v at greater depth, the optimal stress regime for thrust-faulting events. According to Shen et al. (2019), the stress-regime transition occurs between 3.4 and 10.4 km, with the optimal depth at 5.9 km. In addition, the mixture of FMSs might imply the existence of Riedel-shear structures. The presence of Riedel-shear structures, the embryonic stage of strike-slip fault formation (Riedel, 1929), might imply the influence of large-volume fluid injection in the seismotectonic setting. Following the initiation and development of pull-apart basins with Riedel-shear mechanism in laboratory experiments (Atmaoui et al., 2006), the slip surfaces of the strike-slip faults are expected to be on structures at an early stage of development, although potential slip surfaces or zones of weakness must not be newly created.

Use of the GUI allows the analyst to refine the corner frequency from the default fit (Figure 4). In the example shown, the spectral ratio of station RU06 is conspicuously high, MG04 shows an anomaly at 7–10 Hz, and RU01 and

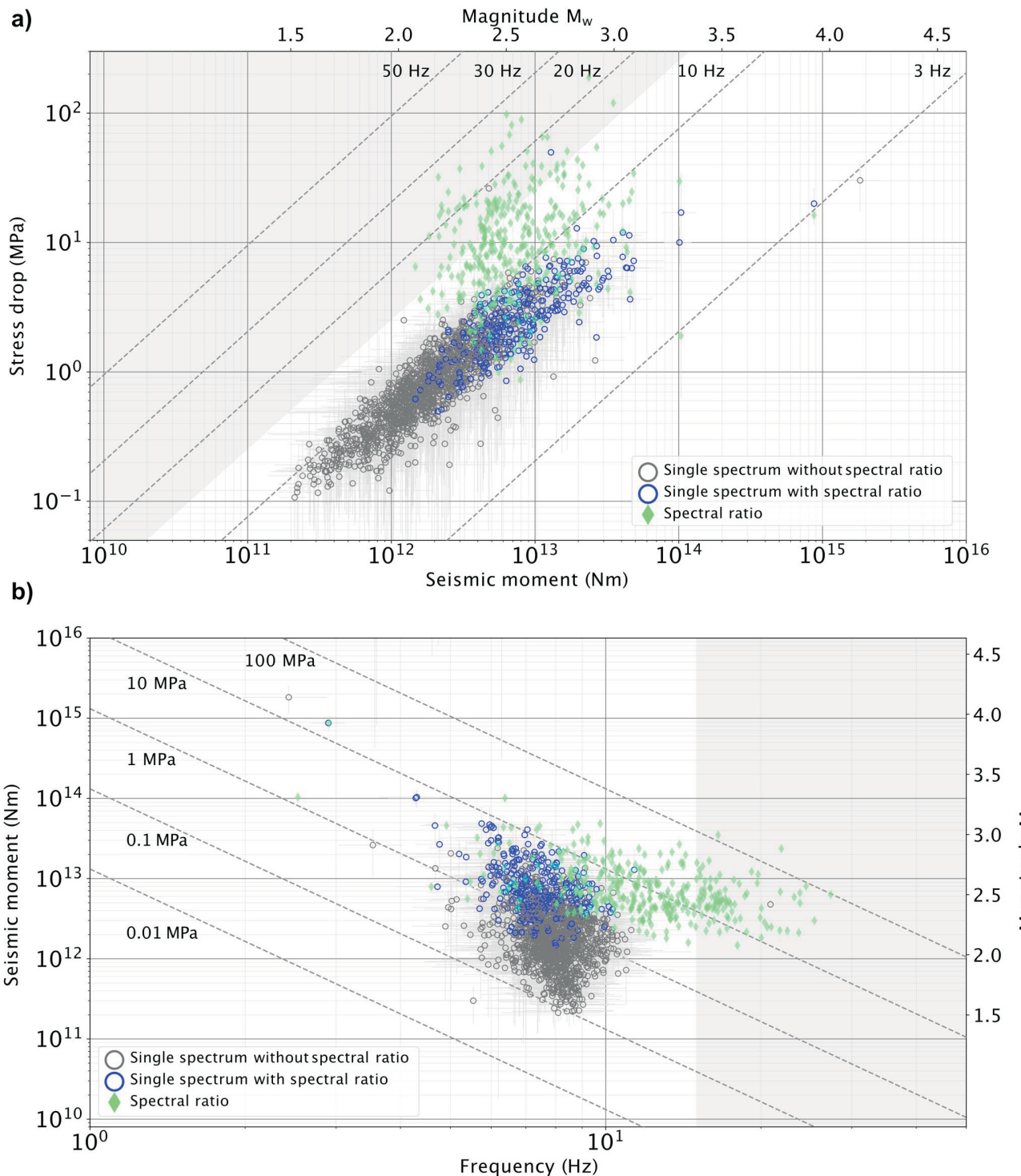


Figure 5. Scaling of stress drop versus seismic moment (a) and seismic moment versus corner frequency (b). In both plots, circles denote solutions from single spectra, the blue circles being those events for which the spectral-ratio method was applied, whereas grey circles do not have a spectral-ratio solution. The green diamonds are the results from spectral ratios. Isolines in part a show constant corner frequencies, whereas isolines in part b highlight the levels of constant stress drops. The grey shading above 15 Hz indicates the area where the corner frequency might not be resolved correctly.

MONT1 are biasing the stacked spectral ratio between 10 and 20 Hz. By removing the individual stations before the fitting process, the corner frequency decreases from 8.32 to 7.63 Hz. Thus, using the GUI enables the processing of a dataset with higher precision compared to automatically determined corner frequencies. In the present case, by inspecting all individual spectral ratios, the analyst is able to investigate in-site effects beneath individual stations (Yang et al., 2009), as the stations are close to the clusters and the HF wells (Figure 1). Variations of individual spectral ratios from the stacked spectral ratio might indicate, for example, the influence of fluid injections.

Comparing the results from single-spectra estimates versus spectral-ratio estimates shows a strong scaling for single-spectra results and a wide range of values for spectral-ratio results, especially for lower-moment magnitudes (i.e., $\sim M_w$ 2.3). A possible reason for this might be the limited frequency band of the dataset (i.e., sampling rate of 100 Hz) and the fact that only surface stations are used, which limits the maximum resolvable corner frequency because the attenuation for higher frequencies is higher (Abercrombie, 1995; Viegas et al., 2010). The same breakdown in constant stress drop is reported from other studies that estimate source parameters with single-spectrum approaches (e.g., Onwuemeka et al., 2018; Kemna et al., 2020). The methods seem to generate the same results when considering events with M_w greater than 3, although the observation is based on few data points. However, a number of studies suggest that spectral ratios provide more reliable estimates of source parameters, particularly for smaller earthquakes, and that they should be preferred over single-spectrum estimates for interpreting scaling with size (e.g., Ide and Beroza, 2001; Ide et al., 2003). Taking the limitation of the magnitude range into account, the stress drop of the induced events in the WCSB may be constant with respect to magnitude, which agrees with the scaling laws for similar events (Aki, 1967) and the repetitive character of induced events in general (Skoumal et al., 2015), which is also observed in the WCSB (Schultz et al., 2015; Roth et al., 2020). This study can be integrated with earlier studies on stress-drop values for induced events in the Montney Formation, specifically 1) results from Yu et al. (2020) that suggest a lower stress drop for events proximal to HF wells (0.1–1 MPa), whereas events distal from HF wells have a higher stress drop (1–10 MPa); and 2) results from Wang (2020) that suggest stress-drop values between 1 and 35 MPa, in the typical range of tectonic earthquakes (0.1–100 MPa; Hanks, 1977). In a broader context, values from this study agree with the average stress drop for small- to moderate-size events in the WCSB, which is 7.5 ± 0.5 MPa (Holmgren et al., 2019).

Acknowledgments

This project is partially funded by the Deutsche Forschungsgemeinschaft (DFG, German Research Foundation, Project Number 428868223), Ruhr University Bochum (RUB) New Faculty start-up funds, and the Natural Sciences and Engineering Research Council of Canada (NSERC) Strategic Partnership Grant for Projects (STPGP) Number 494141-2016. The authors acknowledge H. Kao from Natural Resources Canada (NRCan) and G. Langston, J. Onwuemeka and B. Wang from McGill University for help with seismic-station deployment; S. Venables and BC Oil and Gas Commission (BCOGC) staff for providing well data and logistical support; K.D. Fischer from RUB Seismological Observatory for help with data acquisition; and R. Wache (RUB) for analyzing HF well trajectories. The lead author received support through a Geoscience BC scholarship. H. Yu (NRCan), C. Pellett, C. Salas and A. Babaie Mahani (all Geoscience BC), and B. Davie (RnD Technical) provided reviews that improved the quality of the manuscript.

References

- Abercrombie, R.E. (1995): Earthquake source scaling relationships from –1 to 5 M_L using seismograms recorded at 2.5 km depth; *Journal of Geophysical Research: Solid Earth*, v. 100, no. B12, p. 24015–24036, URL <<https://agupubs.onlinelibrary.wiley.com/doi/abs/10.1029/95JB02397>> [August 2020].
- Abercrombie, R.E. (2014): Stress drops of repeating earthquakes on the San Andreas Fault at Parkfield; *Geophysical Research Letters*, v. 41, no. 24, p. 8784–8791, URL <<https://agupubs.onlinelibrary.wiley.com/doi/full/10.1002/2014GL062079>> [August 2020].
- Abercrombie, R.E. (2015): Investigating uncertainties in empirical Green's function analysis of earthquake source parameters; *Journal of Geophysical Research: Solid Earth*, v. 120, no. 6, p. 4263–4277, URL <<https://agupubs.onlinelibrary.wiley.com/doi/full/10.1002/2015JB011984>> [August 2020].
- Abercrombie, R.E., Poli, P. and Bannister, S. (2017): Earthquake directivity, orientation, and stress drop within the subducting plate at the Hikurangi Margin, New Zealand; *Journal of Geophysical Research: Solid Earth*, v. 122, no. 12, p. 10176–10188, URL <<https://agupubs.onlinelibrary.wiley.com/doi/full/10.1002/2017JB014935>> [August 2020].
- Aki, K. (1967): Scaling law of seismic spectrum; *Journal of Geophysical Research*, v. 72, no. 4, p. 1217–1231, URL <<https://agupubs.onlinelibrary.wiley.com/doi/abs/10.1029/JZ072i004p01217>> [April 2017].
- Aki, K. and Richards, P.G. (2002): Elastic waves from a point dislocation source; Chapter 4 in *Quantitative Seismology* (2nd edition), University Science Books, Sausalito, California, p. 63–117.
- Atkinson, G.M., Eaton, D.W., Ghofrani, H., Walker, D., Cheadle, B., Schultz, R., Shcherbakov, R., Tiampo, K., Gu, J., Harrington, R.M., Liu, Y., van der Baan, M. and Kao, H. (2016): Hydraulic fracturing and seismicity in the Western Canada Sedimentary Basin; *Seismological Research Letters*, v. 87,

- no. 3, p. 631–647, URL <<https://pubs.geoscienceworld.org/ssa/srl/article/87/3/631/315665>> [August 2017].
- Atmaoui, N., Kukowski, N., Stöckhert, B. and König, D. (2006): Initiation and development of pull-apart basins with Riedel shear mechanism: insights from scaled clay experiments; *International Journal of Earth Sciences*, v. 95, no. 2, p. 225–238, URL <<https://link.springer.com/article/10.1007/s00531-005-0030-1>> [October 2020].
- Babaie Mahani, A., Esfahani, F., Kao, H., Gaucher, M., Hayes, M., Visser, R. and Venables, S. (2020): A systematic study of earthquake source mechanism and regional stress field in the southern Montney unconventional play of northeast British Columbia, Canada; *Seismological Research Letters*, v. 91, no. 1, p. 195–206, URL <<https://pubs.geoscienceworld.org/ssa/srl/article/91/1/195/579422>> [January 2020].
- Babaie Mahani, A., Kao, H., Atkinson, G.M., Assatourians, K., Addo, K. and Liu, Y. (2019): Ground-motion characteristics of the 30 November 2018 injection-induced earthquake sequence in northeast British Columbia, Canada; *Seismological Research Letters*, v. 90, no. 4, p. 1457–1467, URL <<https://pubs.geoscienceworld.org/ssa/srl/article/90/4/1457/571681/Ground-Motion-Characteristics-of-the-30-November>> [July 2019].
- Babaie Mahani, A., Schultz, R., Kao, H., Walker, D., Johnson, J. and Salas, C. (2017): Fluid injection and seismic activity in the northern Montney play, British Columbia, Canada, with special reference to the 17 August 2015 Mw 4.6 induced earthquake; *Bulletin of the Seismological Society of America*, v. 107, no. 2, p. 542–552, URL <<https://pubs.geoscienceworld.org/ssa/bssa/article/107/2/542/354161>> [November 2018].
- Barclay, J., Krause, F., Campbell, R. and Utting, J. (1990): Dynamic casting and growth faulting: Dawson Creek graben complex, Carboniferous–Permian Peace River embayment, western Canada; *Bulletin of Canadian Petroleum Geology*, v. 38, no. 1, p. 115–145, URL <<https://pubs.geoscienceworld.org/cspg/bcpge/article/38A/1/115/582791/Dynamic-casting-and-growth-faulting-Dawson-Creek>> [August 2019].
- Boatwright, J. (1978): Detailed spectral analysis of two small New York State earthquakes; *Bulletin of the Seismological Society of America*, v. 68, no. 4, p. 1117–1131, URL <<https://pubs.geoscienceworld.org/ssa/bssa/article/68/4/1117/117843>> [November 2019].
- Brune, J.N. (1970): Tectonic stress and the spectra of seismic shear waves from earthquakes; *Journal of Geophysical Research*, v. 75, no. 26, p. 4997–5009, URL <<https://agupubs.onlinelibrary.wiley.com/doi/abs/10.1029/jb075i026p04997>> [November 2019].
- Brune, J.N. (1971): Correction to tectonic stress and the spectra of seismic shear waves from earthquakes; *Journal of Geophysical Research*, v. 76, no. 20, p. 5002, URL <https://agupubs.onlinelibrary.wiley.com/doi/abs/10.1029/JB076i020p05002> [November 2019].
- Clerc, F., Harrington, R.M., Liu, Y. and Gu, Y. (2016): Stress drop estimates and hypocenter relocations of induced seismicity near Crooked Lake, Alberta; *Geophysical Research Letters*, v. 43, no. 13, p. 6942–6951, URL <<https://agupubs.onlinelibrary.wiley.com/doi/full/10.1002/2016GL069800>> [August 2020].
- Dahm, T., Heimann, S., Funke, S., Wendt, S., Rappel, I., Bindi, D., Plenefisch, T. and Cotton, F. (2018): Seismicity in the block mountains between Halle and Leipzig, central Germany: centroid moment tensors, ground motion simulation, and felt intensities of two M~3 earthquakes in 2015 and 2017; *Journal of Seismology*, v. 22, no. 4, p. 985–1003, URL <<https://link.springer.com/article/10.1007/s10950-018-9746-9>> [September 2020].
- Davies, G.R. (1997): The Triassic of the Western Canada Sedimentary Basin: tectonic and stratigraphic framework, paleogeography, paleoclimate and biota; *Bulletin of Canadian Petroleum Geology*, v. 45, no. 4, p. 434–460, URL <<https://pubs.geoscienceworld.org/cspg/bcpge/article/45/4/434/54206>> [August 2019].
- Eaton, D.W., Ross, G.M. and Hope, J. (1999): The rise and fall of a cratonic arch: a regional seismic perspective on the Peace River Arch, Alberta; *Bulletin of Canadian Petroleum Geology*, v. 47, no. 4, p. 346–361, URL <<https://pubs.geoscienceworld.org/cspg/bcpge/article/47/4/346/57760>> [August 2019].
- Eshelby, J.D. (1957): The determination of the elastic field of an ellipsoidal inclusion, and related problems; *Mathematical and Physical Sciences*, v. 241, no. 1226, p. 376–396, URL <<https://royalsocietypublishing.org/doi/10.1098/rspa.1957.0133>> [November 2019].
- Foulger, G.R., Wilson, M.P., Gluyas, J.G., Julian, B.R. and Davies, R.J. (2018): Global review of human-induced earthquakes; *Earth-Science Reviews*, v. 178, p. 438–514, URL <<https://www.sciencedirect.com/science/article/pii/S00128251730003X>> [August 2020].
- Got, J.L., Fréchet, J. and Klein, F.W. (1994): Deep fault plane geometry inferred from multiplet relative relocation beneath the south flank of Kilauea; *Journal of Geophysical Research: Solid Earth*, v. 99, no. B8, p. 15375–15386, URL <<https://agupubs.onlinelibrary.wiley.com/doi/abs/10.1029/94JB00577>> [August 2017].
- Hanks, T.C. (1977): Earthquake stress drops, ambient tectonic stresses and stresses that drive plate motions; in *Stress in the Earth*, M. Wyss (ed.), Brinkhäuser, Basel, Contributions to Current Research in Geophysics (CCRG), p. 441–458, URL <https://link.springer.com/chapter/10.1007/978-3-0348-5745-1_28> [September 2020].
- Harrington, R.M., Kwiatek, G. and Moran, S.C. (2015): Self-similar rupture implied by scaling properties of volcanic earthquakes occurring during the 2004–2008 eruption of Mount St. Helens, Washington; *Journal of Geophysical Research: Solid Earth*, v. 120, no. 7, p. 4966–4982, URL <<https://agupubs.onlinelibrary.wiley.com/doi/full/10.1002/2014JB011744>> [October 2020].
- Hartzell, S.H. (1978): Earthquake aftershocks as Green's functions; *Geophysical Research Letters*, v. 5, no. 1, p. 1–4, URL <[https://agupubs.onlinelibrary.wiley.com/doi/abs/10.1029/GL005i001p00001@10.1002/\(ISSN\)1944-8007.GRL40>](https://agupubs.onlinelibrary.wiley.com/doi/abs/10.1029/GL005i001p00001@10.1002/(ISSN)1944-8007.GRL40>) [August 2020].
- Heimann, S., Kriegerowski, M., Isken, M., Cesca, S., Daout, S., Grigoli, F., Juretzek, C., Megies, T., Nooshiri, N., Steinberg, A., Sudhaus, H., Vasyura-Bathke, H., Willey, T. and Dahm, T. (2017): Pyrocko – an open-source seismology toolbox and library; GFZ Data Services, URL <<https://datascientific.gfz-potsdam.de/panmetaworks/showshort.php?id=escidoc:2144891>> [November 2019].
- Holmgren, J.M., Atkinson, G.M. and Ghofrani, H. (2019): Stress drops and directivity of induced earthquakes in the Western Canada Sedimentary Basin; *Bulletin of the Seismological Society of America*, v. 109, no. 5, p. 1635–1652, URL <<https://pubs.geoscienceworld.org/ssa/bssa/article/109/5>>

- 1635/573126/Stress-Drops-and-Directivity-of-Induced> [June 2020].
- Ide, S. and Beroza, G.C. (2001): Does apparent stress vary with earthquake size?; *Geophysical Research Letters*, v. 28, no. 17, p. 3349–3352, URL <<https://agupubs.onlinelibrary.wiley.com/doi/abs/10.1029/2001GL013106>> [October 2020].
- Ide, S., Beroza, G.C., Prejean S.G. and Ellsworth W.L. (2003): Apparent break in earthquake scaling due to path effects on deep borehole recordings; *Journal of Geophysical Research: Solid Earth*, v. 108, no. B5, URL <<https://agupubs.onlinelibrary.wiley.com/doi/full/10.1029/2001JB001617>> [October 2020].
- Kaneko, Y. and Shearer, P.M. (2014): Seismic source spectra and estimated stress drop derived from cohesive-zone models of circular subshear rupture; *Geophysical Journal International*, v. 197, no. 2, p. 1002–1015, URL <<https://academic.oup.com/gji/article/197/2/1002/617325>> [August 2020].
- Kemna, K.B., Peña Castro, A.F., Harrington, R.M. and Cochran, E.S. (2020): Using a large-n seismic array to explore the robustness of spectral estimations; *Geophysical Research Letters*, v. 47, no. 21, URL <<https://doi.org/10.1029/2020GL089342>>.
- Ko, Y.T., Kuo, B.Y. and Hung, S.H. (2012): Robust determination of earthquake source parameters and mantle attenuation; *Journal of Geophysical Research: Solid Earth*, v. 117, no. B4, URL <<https://agupubs.onlinelibrary.wiley.com/doi/full/10.1029/2011JB008759>> [October 2020].
- Kwiatek, G., Bulut, F., Bohnhoff, M. and Dresen, G. (2014): High-resolution analysis of seismicity induced at Berlin geothermal field, El Salvador; *Geothermics*, v. 52, p. 98–111, URL <<https://www.sciencedirect.com/science/article/pii/S0375650513000825>> [October 2020].
- Lei, X., Wang, Z. and Su, J. (2019): The December 2018 ML 5.7 and January 2019 ML 5.3 earthquakes in South Sichuan basin induced by shale gas hydraulic fracturing; *Seismological Research Letters*, v. 90, no. 3, p. 1099–1110, URL <<https://pubs.geoscienceworld.org/ssa/srl/article/90/3/1099/569798/The-December-2018-ML-5-7-and-January-2019-ML-5-3>> [September 2019].
- McGarr, A., Bekins, B., Burkhardt, N., Dewey, J., Earle, P., Ellsworth, W., Ge, S., Hickman, S., Holland, A., Majer, E. and Rubinstein, J. (2015): Coping with earthquakes induced by fluid injection; *Science*, v. 347, no. 6224, p. 830–831, URL <<https://science.scienmag.org/content/347/6224/830.summary>> [August 2018].
- Onwuemeka, J., Harrington, R.M., Liu, Y. and Kao, H. (2019): Source properties of earthquakes around hydraulic-fracturing sites near Dawson Creek, northeastern British Columbia; in *Geoscience BC Summary of Activities 2018: Energy and Water*, Geoscience BC, Report 2019-02, p. 63–66, URL <http://cdn.geosciencebc.com/pdf/SummaryofActivities2018/EW/Schol_SoA2018_EW_Onwuemeka.pdf> [September 2019].
- Onwuemeka, J., Liu, Y. and Harrington, R.M. (2018): Earthquake stress drop in the Charlevoix seismic zone, eastern Canada; *Geophysical Research Letters*, v. 45, no. 22, p. 12226–12235, URL <<https://agupubs.onlinelibrary.wiley.com/doi/full/10.1029/2018GL079382>> [August 2020].
- Pană, D.I. and van der Pluijm, B.A. (2015): Orogenic pulses in the Alberta Rocky Mountains: radiometric dating of major faults and comparison with the regional tectono-stratigraphic record; *Geological Society of America Bulletin*, v. 127, no. 3/4, p. 480–502, URL <<https://pubs.geoscience-world.org/gsa/gsabulletin/article/127/3-4/480/126124>> [August 2019].
- Peña Castro, A.F., Roth, M.P., Verdecchia, A., Onwuemeka, J., Liu, Y., Harrington, R.M., Zhang, Y. and Kao, H. (2020): Stress chatter via fluid flow and fault slip in a hydraulic fracturing-induced earthquake sequence in the Montney formation, British Columbia; *Geophysical Research Letters*, v. 47, no. 14, URL <<https://agupubs.onlinelibrary.wiley.com/doi/full/10.1029/2020GL087254>> [July 2020].
- Prieto, G.A., Parker, R.L. and Vernon III, F.L. (2009): A Fortran 90 library for multitaper spectrum analysis; *Computers & Geosciences*, v. 35, no. 8, p. 1701–1710, URL <<https://www.sciencedirect.com/science/article/pii/S0098300409000077>> [August 2020].
- Prieto, G.A., Thomson, D.J., Vernon, F.L., Shearer, P.M. and Parker, R.L. (2007): Confidence intervals for earthquake source parameters; *Geophysical Journal International*, v. 168, no. 3, p. 1227–1234, URL <<https://academic.oup.com/gji/article/168/3/1227/931413>> [August 2020].
- Riedel, W. (1929): Zur Mechanik geologischer Bruchscherungen ein Beitrag zum Problem der Fiederspalten; *Zentralblatt Mineral. Paläont.*, p. 354–368.
- Ross, Z.E. and Ben-Zion, Y. (2016): Toward reliable automated estimates of earthquake source properties from body wave spectra; *Journal of Geophysical Research: Solid Earth*, v. 121, no. 6, p. 4390–4407, URL <<https://agupubs.onlinelibrary.wiley.com/doi/full/10.1002/2016JB013003>> [August 2020].
- Ross, Z.E., Ben-Zion, Y., White, M.C. and Vernon, F.L. (2016): Analysis of earthquake body wave spectra for potency and magnitude values: implications for magnitude scaling relations; *Geophysical Journal International*, v. 207, no. 2, p. 1158–1164, URL <<https://academic.oup.com/gji/article/207/2/1158/2583777>> [May 2019].
- Roth, M.P., Verdecchia, A., Harrington, R.M. and Liu, Y. (2020): High-resolution imaging of hydraulic-fracturing-induced earthquake clusters in the Dawson-Septimus area, northeast British Columbia, Canada; *Seismological Research Letters*, v. 91, no. 5, p. 2744–2756, URL <<https://pubs.geoscience-world.org/ssa/srl/article/91/5/2744/588077/High-Resolution-Imaging-of-Hydraulic-Fracturing>> [July 2020].
- Ruhl, C.J., Abercrombie, R.E. and Smith, K.D. (2017): Spatiotemporal variation of stress drop during the 2008 Mogul, Nevada, earthquake; *Journal of Geophysical Research: Solid Earth*, v. 122, no. 10, p. 8163–8180, URL <<https://agupubs.onlinelibrary.wiley.com/doi/full/10.1002/2017JB014601>> [August 2020].
- Ruscic, M., Bocchini, G.M., Becker, D., Meier, T. and van Keken, P.E. (2019): Variable spatio-temporal clustering of microseismicity in the Hellenic subduction zone as possible indicator for fluid migration; *Lithos*, v. 346, p. 105154, URL <<https://www.sciencedirect.com/science/article/abs/pii/S0024493719303056>> [August 2019].
- Schultz, R., Stern, V., Novakovic, M., Atkinson, G. and Gu, Y.J. (2015): Hydraulic fracturing and the Crooked Lake sequences: insights gleaned from regional seismic networks; *Geophysical Research Letters*, v. 42, no. 8, p. 2750–2758, URL <<https://agupubs.onlinelibrary.wiley.com/doi/full/10.1002/2015GL063455>> [April 2020].

- Shen, L.W., Schmitt, D.R. and Haug, K. (2019): Quantitative constraints to the complete state of stress from the combined borehole and focal mechanism inversions: Fox Creek, Alberta; *Tectonophysics*, v. 764, p. 110–123, URL <<https://www.sciencedirect.com/science/article/abs/pii/S0040195119301477>> [May 2020].
- Skoumal, R. J., Brudzinski, M.R. and Currie, B.S. (2015): Distinguishing induced seismicity from natural seismicity in Ohio: demonstrating the utility of waveform template matching; *Journal of Geophysical Research*, v. 120, no. 9, p. 6284–6296, URL <<https://agupubs.onlinelibrary.wiley.com/doi/full/10.1002/2015JB012265%4010.1002/%28ISSN%291944-8007.FRACKING>> [April 2020].
- Viegas, G., Abercrombie, R.E. and Kim, W.Y. (2010): The 2002 M5 Au Sable Forks, NY, earthquake sequence: source scaling relationships and energy budget; *Journal of Geophysical Research*, v. 115, no. B7, URL <<https://agupubs.onlinelibrary.wiley.com/doi/full/10.1029/2009JB006799>> [August 2020].
- Wang, B., Harrington, R.M., Liu, Y., Kao, H. and Yu, H. (2020): A study on the largest hydraulic-fracturing-induced earthquake in Canada: observations and static stress-drop estimation; *Bulletin of the Seismological Society of America*, URL <<https://pubs.geoscienceworld.org/ssa/bssa/article/110/5/2283/587916/A-Study-on-the-Largest-Hydraulic-Fracturing>> [July 2020].
- Wang, R. (1999): A simple orthonormalization method for stable and efficient computation of Green's functions; *Bulletin of the Seismological Society of America*, v. 89, no. 3, p. 733–741, URL <<https://pubs.geoscienceworld.org/ssa/bssa/article/89/3/733/120414>> [September 2020].
- Yang, W., Peng, Z. and Ben-Zion, Y. (2009): Variations of strain-drops of aftershocks of the 1999 Izmit and Düzce earthquakes around the Karadere-Düzce branch of the North Anatolian Fault; *Geophysical Journal International*, v. 177, no. 1, p. 235–246, URL <<https://academic.oup.com/gji/article/177/1/235/729018>> [September 2020].
- Yu, H., Harrington, R.M., Kao, H., Liu, Y., Abercrombie, R.E. and Wang, B. (2020): Well proximity governing stress drop variation and seismic attenuation associated with hydraulic fracturing induced earthquakes; *Journal of Geophysical Research: Solid Earth*, v. 125, no. 9, URL <<https://agupubs.onlinelibrary.wiley.com/doi/full/10.1029/2020JB020103>> [September 2020].

